Acta Materialia 165 (2019) 388–397

Contents lists available at ScienceDirect

Acta Materialia

journal homepage: www.elsevier.com/locate/actamat

Full length article

In situ high speed imaging study and modelling of the fatigue fragmentation of dendritic structures in ultrasonic fields

S. Wang [a], J. Kang [a, b, **], Z. Guo [a, *], T.L. Lee [c, d], X. Zhang [a], Q. Wang [a], C. Deng [a], J. Mi [d]

[a] School of Materials Science and Engineering, Tsinghua University, Beijing, China
[b] Key Laboratory for Advanced Materials Processing Technology, Ministry of Education, China
[c] ISIS Neutron Source, STFC Rutherford Appleton Laboratory, Harwell Campus, Didcot, Oxfordshire, OX11 0QX, UK
[d] School of Engineering and Computer Science, University of Hull, Cottingham Road, Hull, HU6 7RX, UK

ARTICLE INFO

Article history:
Received 12 June 2018
Received in revised form
15 October 2018
Accepted 28 November 2018
Available online 5 December 2018

Keywords:
Dendrites fragmentation
Ultrasonic bubble
Ultrasound
Oscillation
Fatigue crack

ABSTRACT

The fatigue fragmentation of dendritic structures of a SCN-5*wt.*% Camphor transparent alloy in an ultrasound field was investigated systematically using high-speed imaging. Dynamic interactions between oscillating ultrasonic bubbles and the primary and secondary dendrites were observed and recorded. High speed images show that when an ultrasound bubble was trapped inside an interdendritic region, the oscillation of the bubble can cause cyclic bending of the dendritic arms. Consequently, a fatigue type crack initiated at the arm root and propagated through the dendrite, causing the dendrite to fragment, i.e. dendritic fragmentation. From the recorded videos, the cycle numbers for the fatigue fragmentation were extracted, then, the fatigue strength and fatigue life of the SCN-5*wt.*% Camphor transparent alloy were calculated. Results showed that the cyclic fatigue load cause a crack initiating on a SCN dendrite at a much lower stress level than its tensile strength under high frequent oscillation.

1. Introduction

For many years, ultrasound treatment (UST) has been demonstrated to be effective in refining the microstructures of metallic alloys during solidification [1–5]. The proposed mechanisms of grain refinement due to ultrasound are enhanced homogenous and/or heterogeneous nucleation [6–8], and dendrite fragmentation [1,2]. Hunt [6] was probably among the first to propose that bubble implosion in a solidifying melt could increase the undercooling of nearby melt, leading to an enhanced homogenous nucleation rate. However, it is very difficult to validate such assumption experimentally. Many experimental studies have indeed confirmed the enhanced heterogeneous nucleation effects due to activation of the potent nucleating particles in a liquid melt [9–12], e.g. Al_2O_3 particles in an Al alloy melt. Dendrite fragmentation is mainly the fragmentation and detachment of primary, secondary or even tertiary dendritic arms, which then act as the new seed grains to create a grain multiplication effect. In solidification conditions without a strong convection, dendrite fragmentation could be also caused by the thermosolutal effects [13–16], For example Ruvalcaba et al. [13] observed the dendritic fragmentation of an Al-20 wt%Cu alloy using synchrotron X-radiation microscopy. It was found that the local solute-enrichment caused remelting of dendrite root and then the detachment occurred. Nagira et al. [14] reported that ultrasound field promoted solute transport in the mushy region and then facilitated the fragmentation of Sn dendrites. The mechanism of dendrite root melting induced by the flow of solute-rich liquid under a pulsed electromagnetic field were also observed and reported in Refs. [15,16].

The phenomena of dendrite fragmentation in an ultrasonic field have been well studied recently by using high speed imaging either in transparent organic analogue alloys [17–20] or real metallic alloys using synchrotron X-ray [9,16–20]. For example, Chow et al. studied the fragmentation of ice dendrites and observed a microcrack initiated in an ice crystal under the effect of ultrasound induced bubbles [18]. However, the image acquisition rate (1 *fps*) was too low to give any useful dynamic information. Shu et al. and Wang et al. observed the interactions between ultrasonic bubbles and SCN dendrites by much higher imaging acquisition rate (8113 *fps* and 40,000 *fps* respectively) [19,20]. They found that the

* Corresponding author.
** Corresponding author. School of Materials Science and Engineering, Tsinghua University, Beijing, China.
E-mail addresses: kangjw@tsinghua.edu.cn (J. Kang), zhipeng_guo@mail.tsinghua.edu.cn (Z. Guo).

https://doi.org/10.1016/j.actamat.2018.11.053

dendrite fragmentation was attributed to the force generated by the ultrasonic bubbles, but no crack were observed due to insufficient dendrite magnification at high capture speed. Using synchrotron X-ray radiography, Wang et al. [21] also observed the fragmentation of Al_2Cu intermetallic induced by acoustic streaming flow.

Yang et al. [22] calculated the stress concertation occurred at dendrite roots under stirring forces, and attributed the dendritic fragmentation to the decrease of melting point at root under stress concertation. Tan et al. [23] simulated the stress distribution of a dendrite under cyclic force, and attributed the stress concentration to the fragmentation of dendrite arms at the root. Wang et al. [24] also observed the fatigue crack happened on an Al_3Ti intermetallic phase induced by oscillating ultrasonic bubbles in water. The fragmentation mechanism is via fatigue crack growth under the vibrating effect of pulsating ultrasonic bubbles in a high-frequency cycle on Al_3Ti intermetallic phase. However, the experiment was carried out in water, and the Al_3Ti intermetallic phase was obtained by deep etching the solidified sample. So this experiment was different from the *in situ* observation of microstructure fragmentation in ultrasonic field during solidification.

Very recently, high speed X-ray imaging was used to investigate both ultrasonic bubble dynamics [23,25–27] and the effect of oscillating bubble on solidifying microstructures [21,25]. Wang et al. [25], Tan et al. [26] and Mi et al. [27] performed an ultrafast X-ray imaging study of ultrasonic bubble dynamics (with an image frame rate of 135,780) in the sector 32-ID of the Advanced Photon Source, Argonne National Laboratory, USA. Such imaging acquisition rate capture clearly the dynamics of bubble implosion and oscillation, and their interaction with solid phases. However, due to the limited view field at very high image acquisition speed, it is impossible to view dendrite (normally in a few hundred of micrometers) and bubble (a few tens of micrometers) in the same view field. At relatively slow image acquisition speed, 1000–6000 fps, Wang et al. [21] captured the fragmentation of primary intermetallic particles in an Al-35 *wt*% Cu alloy induced by ultrasound. Wang et al. [25] studied the microstructure fragmentation in a Bi-8*wt*.% Zn alloy in beamline I12 at DLS. Both of them observed the microstructure fragmentation, but no details were reveal due to the lower capture speed in ultrasonic field. Again it is very difficult to allow a growing dendrite and ultrasonic bubbles to be in the same view field at ultrahigh speed such as >20,000 *fps*.

Ultrasound usually works at a high frequency of ~20 kHz. Most of the Synchrotron X-ray sources cannot provide the imaging acquisition speed higher than 20,000 fps (for ultrasound process). As a results, until now, there has been no report on systematic and real-time study that is dedicated to the direct observation of how ultrasonic bubbles interact with growing dendrites in real metallic alloy systems.

Hence, we developed a specific experiment setup to observe the dendrite fragmentation of a transparent SCN-5*wt*. % Camphor alloy using a high speed camera operating at an imaging acquisition speed of 40,000 *fps*. With this acquisition speed, two images per ultrasound cycle can be recorded and the expansion and contraction of an ultrasonic bubble could be observed, and so did the cyclic motion of dendrites driven by the oscillating bubbles. Although its physical properties of SCN-5*wt*.% camphor are different from liquid metal alloys at some extent [25], it is still a very useful alternative model system for the study of the ultrasound treatment during solidification because of the difficulty of achieving the sufficient temporal and spatial resolution at the same time using X-ray to image any liquid metals.

In this paper, the initiation and propagation of the fatigue crack induced by an oscillating bubble were systematically investigated *in situ* and in real-time. The *S-N* curve for the SCN dendrite was also calculated to provide robust and unambiguous information for understanding the fatigue induced crack and fragmentation of primary and secondary dendrites under ultrasound treatment.

2. Experimental

A similar experiment setup as detailed in Ref. [20] was used in this study, as shown in Fig. 1. The experiment cell consisted of two connected chambers. Chamber 1 is for accommodating the sonotrode and introducing ultrasonic wave. Chamber 2 is for viewing dendrite growth and interaction between dendrites and ultrasonic bubbles. Such experiment setup is able to create a relative stable ultrasonic pressure field in the region where dendrites are growing. In this way, the quasi-static oscillation of ultrasonic bubbles can be achieved and maintained in the chamber 2, and then the interaction between dendrite and ultrasound bubbles could be monitored and recorded.

A SCN-5*wt*. % camphor alloy was used, and it was made by melting pure SCN (99 *wt* %) and pure camphor (99.7 *wt* %) in a sealed glass bottle at 343 K (the melting point of SCN-5*wt*. % Camphor is ~325 K) for 30 min. The experiment cell was then filled with the alloy and mounted onto a 3-D observation platform where a high speed camera was also mounted. A predefined thermal gradient (~100 K/m) was imposed to control the temperature so that the dendrites grew horizontally from left to right. A SONICS VCX 150 ultrasound device with a fixed frequency 20 kHz was used. Its power was adjustable from 0 W to 150 W. In experiment, the ultrasound power used was 30 W, and the diameter of the sonotrode tip was 2 mm. A Nac HX-6 high-speed digital video camera (with a magnification of 800 times), manufactured by Nac Image Technology in Tokyo, was used for imaging and recording. The imaging field of view was 256×256 pixel^2 with a spatial resolution of ~1.2 μm/pixel. The imaging acquisition rate used was 40,000 *fps*.

3. Result and discussion

3.1. Dendritic fragmentation in ultrasound field

Fig. 2 shows the fragmentation of both primary and secondary arms by an ultrasonic bubble. As shown in Fig. 2a, several secondary arms bended after an ultrasonic bubble touched the dendrite. These arms oscillated in the same frequency as the ultrasonic bubble (see Fig. 2b) and then fragmented and detached from the primary trunk at 14.175 ms. Similarly, as shown in Fig. 2c, the primary arm oscillated when a ultrasonic bubble of ~120 μm in diameter came in contact. The oscillation became more intense at certain time between Fig. 3d and e when the secondary arms detached, after that the oscillating ultrasonic bubble moved into an interdendritic region (see Fig. 2f). As the primary arm oscillated back and forth, the secondary arms detached after 14 ms, the detail was shown in Fig. 3c and d. After contact with the ultrasound bubble, the dendrite broke about 40 ms later. Clearly, the oscillating bubble imposed a cyclic force onto the dendrites. The detailed fragmentation process can be seen more vividly in video 1 of the supplementary material.

Supplementary video related to this article can be found at https://doi.org/10.1016/j.actamat.2018.11.053.

3.2. The fatigue-crack induced dendritic fragmentation

Fig. 3a shows the fragmentation of a primary arm induced by an ultrasonic bubble as a result of the fatigue effect. As shown in Fig. 3a$_1$, a secondary arm was fragmented and detached from its primary trunk, leaving a scar on the primary arm (as marked by the dash lines in Fig. 3a$_2$). A crack was then initiated at the scar in 0.15 ms. The primary arm oscillated back and forth and finally broke

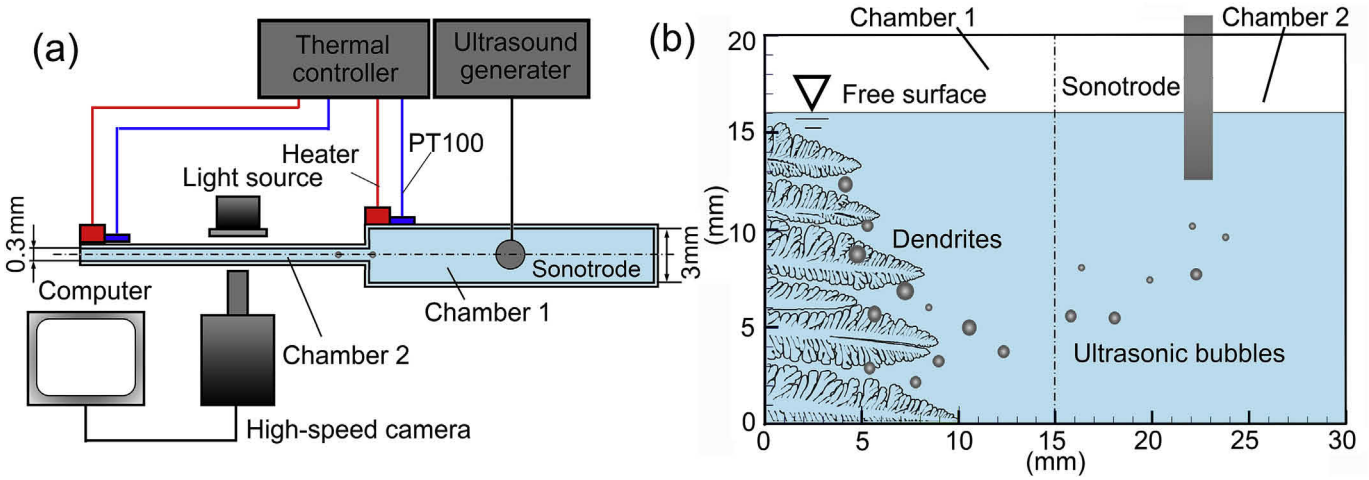

Fig. 1. A schematic illustration of (a) the experimental setup (a top view), and (b) the ultrasonic bubbles generated by a sonotrode positioned ahead of the growing dendrites originated from the left (a front view).

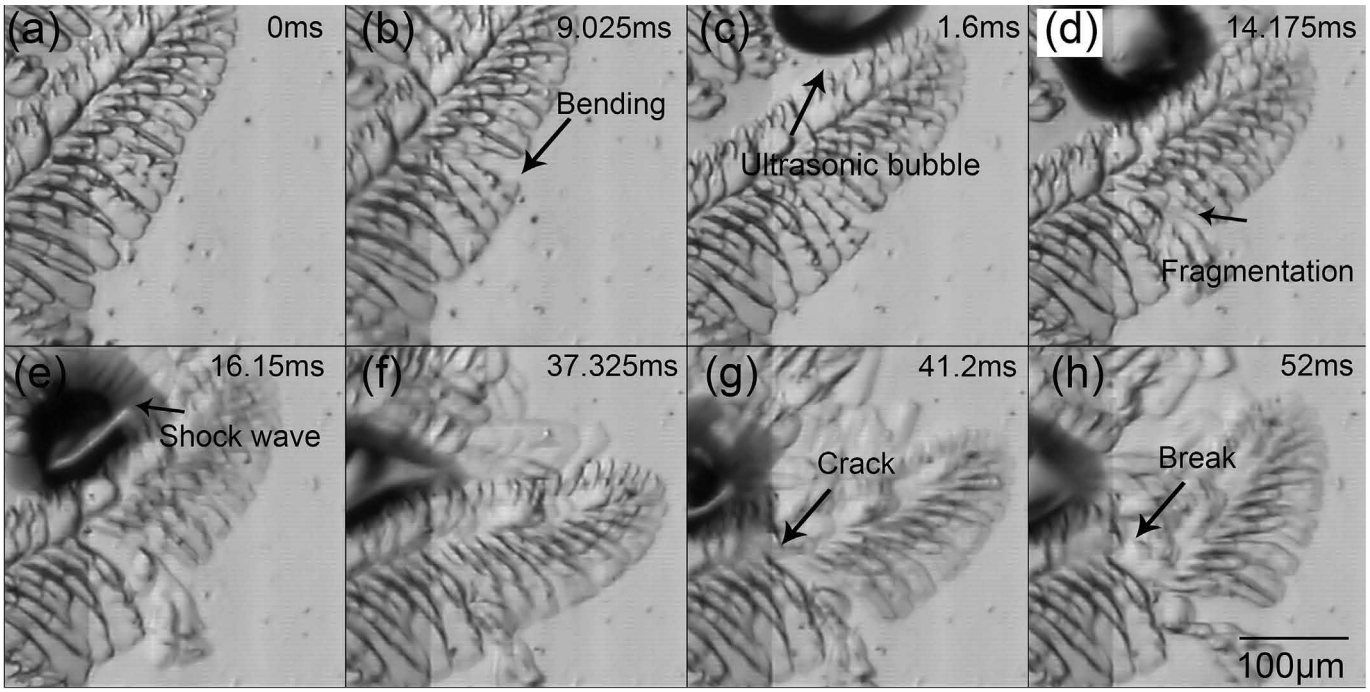

Fig. 2. Fragmentation of the secondary and primary arms caused by an incoming ultrasonic bubble. The ultrasonic power used was 30 W and the image acquisition rate was 40,000 *fps*. The field of view was 302.33 × 302.33 μm^2 and the thermal gradient was 110 K/m.

at about 14.2 ms, the detail can be seen more clearly in supplementary video 2.

Supplementary video related to this article can be found at https://doi.org/10.1016/j.actamat.2018.11.053.

Fig. 3b shows another case of dendritic fragmentation due to the fatigue effect. As shown in Fig. 3b_1-b_2, an ultrasonic bubble B1 of ~80 μm oscillated and collapsed into numerous smaller bubbles. Meanwhile cracks initiated at the dendrite root (see Fig. 3b_3). Fig. 3b_4-b_5 show that the cracks continued to propagate, and finally fragmented arm A1. Cracks also initiated at the root of arm A2 when a new ultrasonic bubble B2 oscillated there (see Fig. 3b_6). Further propagation of the crack led to the detachment of arm A2 (see Fig. 3b_7-b_8). Fig. 3b_9 shows a new ultrasonic bubble came into the view field, oscillating with the same frequency as ultrasonic bubble B2. Mini cracks were observed to initiate inside the crystal after the bubble oscillated for about 130 ms. This fragmentation process can be seen in supplementary video 3.

Supplementary video related to this article can be found at https://doi.org/10.1016/j.actamat.2018.11.053.

Fig. 4 shows the crack formation and propagation in a secondary dendrite arm. An oscillating ultrasonic bubble of 20 μm moved to the root of arm 1 (see Fig. 4a and b). A crack then formed at the root (see Fig. 4b), afterward arm 1detached from the main arm as a debris (see Fig. 4c). It took about 30 ms for the dendrite fragmentation, then, the ultrasonic bubble was flushed away by the melt. As shown in Fig. 4a–c, dendrite arm 2 moved upwards due to the convection induced by the ultrasonic. The bending angle of arm 2 increased to 3.8°, then it started to bend towards arm 1 and the angle increased to 24° (see Fig. 4d and e). As the bending angle increased, a crack initiated and grew at the root of arm 2 (see Fig. 4e).

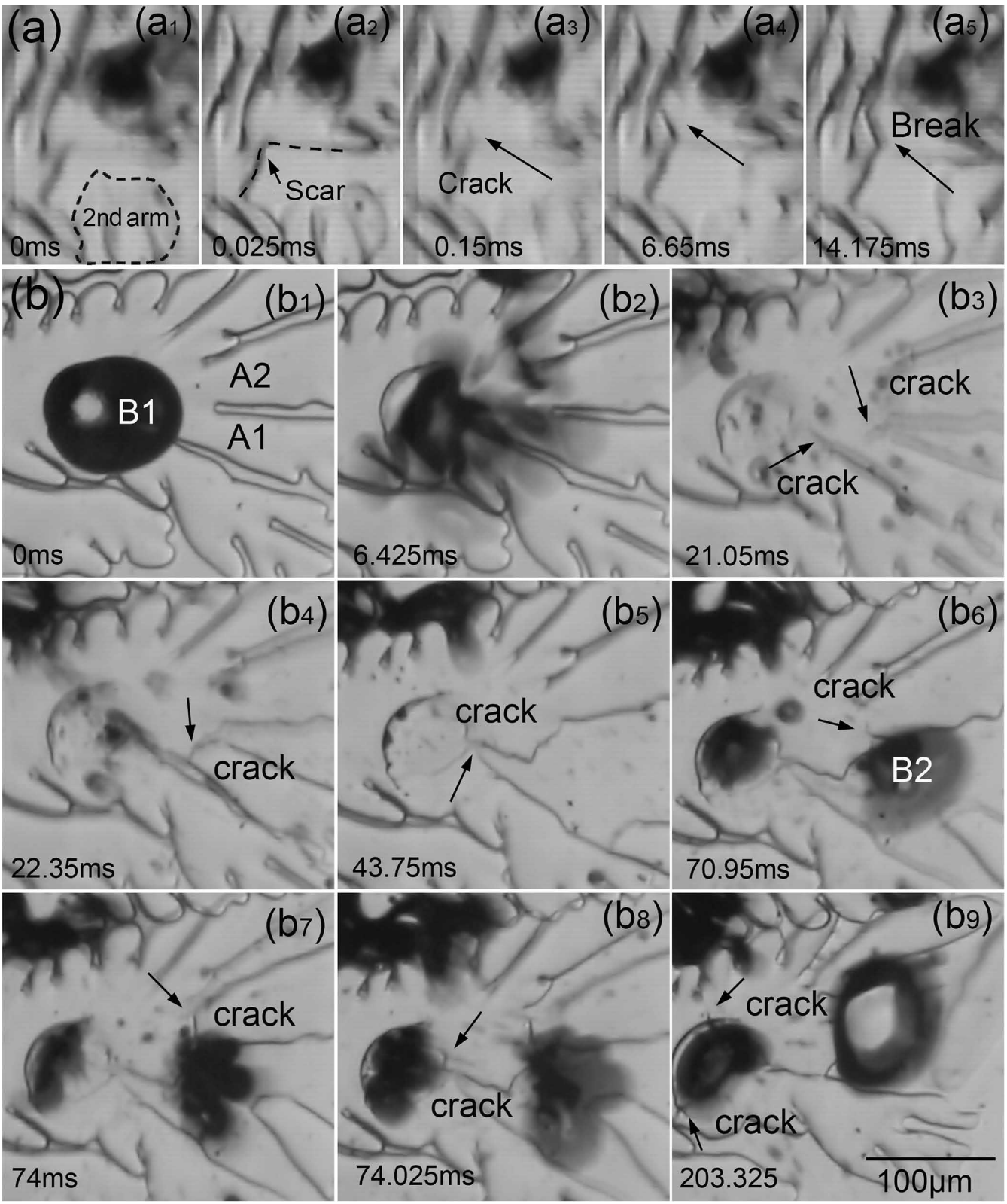

Fig. 3. (a_1) - (a_5) show the fragmentation process of a primary dendrite arm due to the cyclic fatigue effect induced by an ultrasonic bubble. (b_1) - (b_9) show another example of dendritic fragmentation due to a fatigue crack. The ultrasonic power used was 30 W and the image acquisition rate was 40,000 *fps*. The thermal gradient was 153.33 K/m for Fig. 3a and 100 K/m for Fig. 3b. More detailed and vivid information can be seen from the supplementary videos 2 and 3.

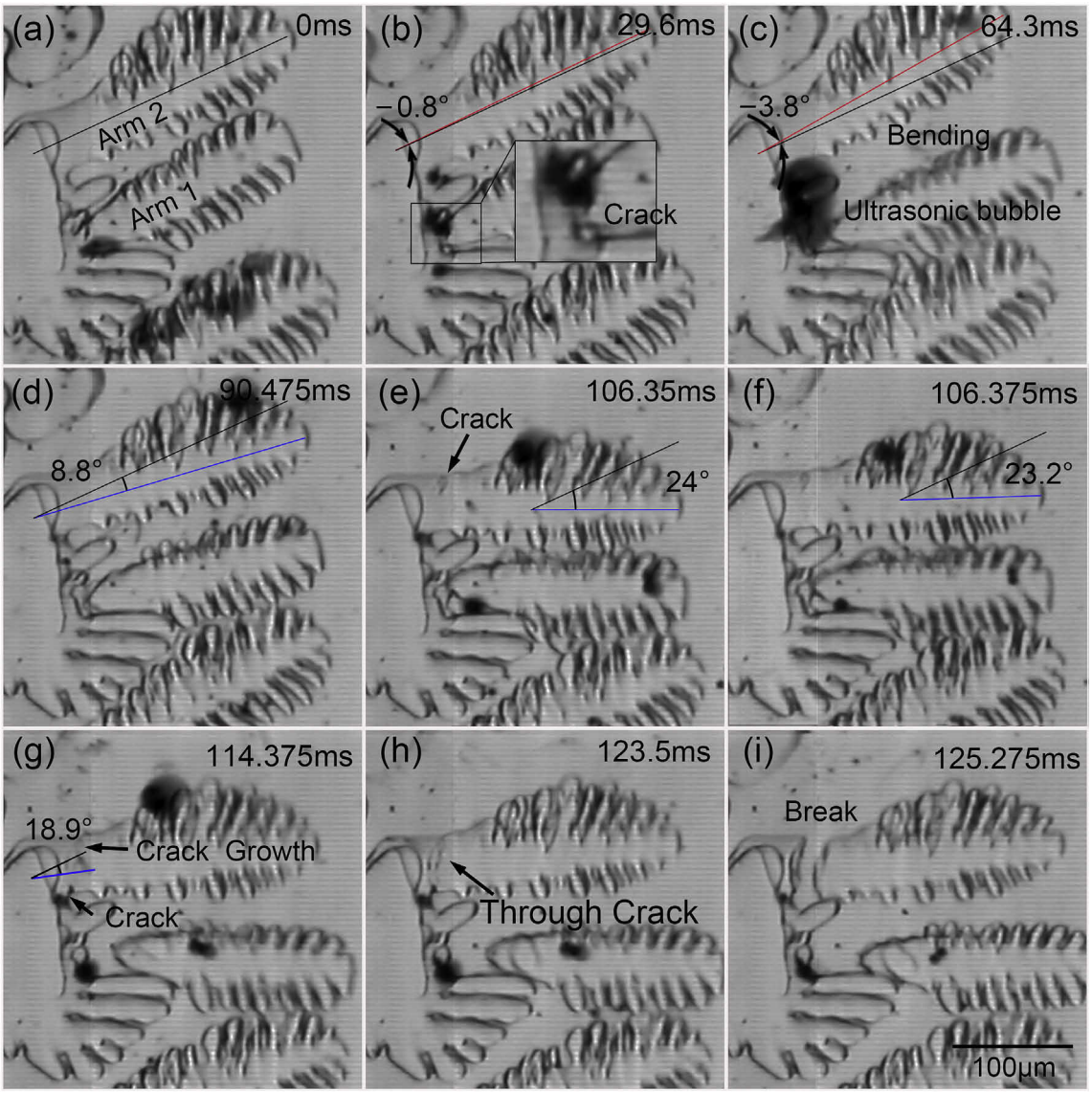

Fig. 4. (a)–(c) show the bending and initiation of a crack at the root of a primary dendrite (Arm 1) after interacting with an oscillating bubble. (d)–(i) show the continuous bending until fragmentation of Arm 2 caused by the fatigue effect induced by the oscillating bubble. The black and blue lines drawn on Arm 2 represent the directions of the primary dendrite arm axis before and after bending; and the angle between the two lines was the bending angle. The ultrasonic power used was 30 W with an image acquisition rate of 40,000 *fps*. The field of view was $302.33 \times 302.33\ \mu m^2$ and the thermal gradient was 100 K/m. (For interpretation of the references to colour in this figure legend, the reader is referred to the Web version of this article.)

Fig. 4e and f showed two consecutive frames in one ultrasonic period. The ultrasonic bubble in Fig. 4e extracted as clearly showed in Fig. 4f, and the angle decreased from 24° to 23.2° due to the motion of the ultrasonic bubble. This indicating that the dendrite arm 2 was under a cyclic movement with the same frequency as the bubble oscillation, and the amplitude angle is about 0.4°. This cyclic movement of the dendrite arm can be seen more clearly in the supplement video 4. As shown in Fig. 4f–g, the ultrasonic bubble started to move away from the dendrite arm, then, arm 2 rotated backwards with a bending angle of 18.9°. Meanwhile, another crack formed at the downside of the root of arm 2 (see Fig. 4g). Both cracks grew into the arm from the surface (seen in Fig. 4g and h) until the detachment occurred at about 125 ms (see Fig. 4i). It takes less than 20 ms for the dendritic fragmentation form the crack initiation to totally running through the dendritic root.

Supplementary video related to this article can be found at https://doi.org/10.1016/j.actamat.2018.11.053.

Fig. 5a and b showed the initiation (stage I) and propagation (stage II) of a crack as a function of the ultrasound cycle number for a primary (orange triangle) and a secondary (green diamond) dendrite arm showed in Fig. 3. For the primary arm, the crack initiated when a secondary arm was detached after about 130 cycles of bending action. Apparently, the crack propagated faster in the 130–140 ultrasonic cycles (stage I) to a length of ~10 μm, and then grew relatively slower in the 140–240 ultrasound cycles until totally fragmented. The primary arm was fragmented in ~110 ultrasound cycles. For the secondary arm, similar phenomenon was observed, and it took ~70 ultrasonic cycles for fragmentation was. It should be noted that, the dendrites were always in cyclic bending motion, and the crack growth process was fast and the imaging acquisition speed of 40,000 *fps* is just about the lower limit that can capture the initiation and growth of the crack.

Fig. 5c showed the bending angle of an oscillating dendrite arm and the crack length as a function of the ultrasound cycle number

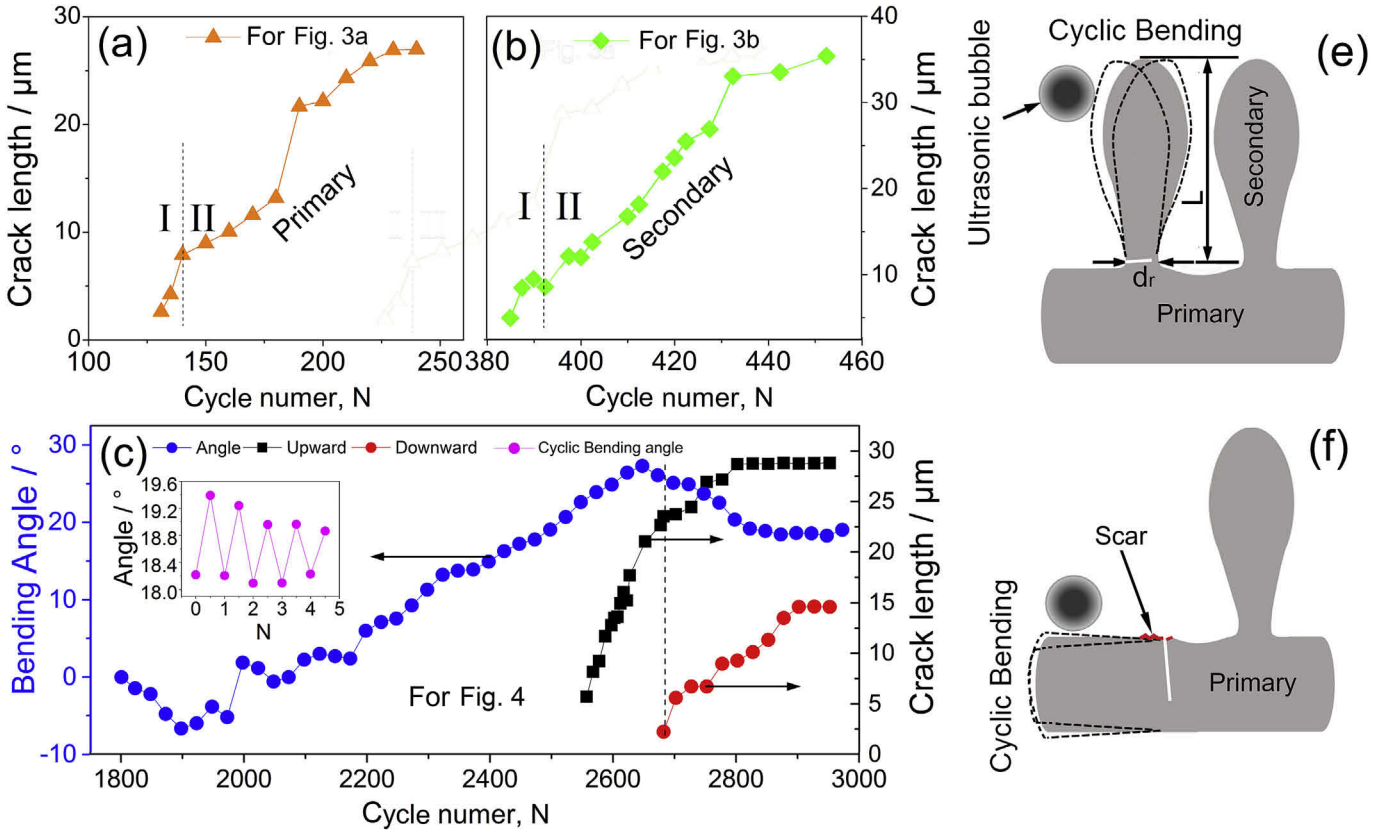

Fig. 5. The growing crack length as a function of ultrasonic bubble oscillating cycles for the fragmented dendrites shown in Figs. 3 and 4. (a) for Fig. 3a and (b) for Fig. 3b and (c) for Fig. 4; (e)–(f) Schematic illustration, showing the cyclic bending effect due to an oscillating bubble. (e) is for the secondary arm and (f) is for the primary arm.

showed in Fig. 4. It is interesting to see that, the dendrite arm was bending back and forth continuously due to the fluid convection in the ultrasound field, and the bending angle increased almost linearly with the increase of the ultrasound cycles, except the initial 1900 cycles. After an oscillating bubble came and touched the dendrite, a crack initiated after ~2550 cycles, and the bending angle increased continuously and almost linearly until the bending motion was restricted by a small neighbor arm. The upside crack length at the arm root increased and a new downside crack initiated as the arm bent backwards; and then both cracks grew inwards together. However, the upside crack stopped growing after ~2800 cycles, but the downside crack continuously grew until 2900 cycles. The total cycle number was ~350 from crack initiation to fragmentation. In addition, the insert graph in Fig. 5c showed the cyclic bending of arm 2 (see Fig. 4) with an amplitude of ~0.4° in 5 cycles. Fig. 5e and f showed a schematic illustration for the cyclic bending for a secondary arm and primary arm, respectively. The arm bent in the same frequency as the ultrasonic bubble. A crack nucleated at the root of the secondary arm and ultimately led to the fragmentation, afterwards such crack location became a week point from where a new crack nucleated on the primary arm.

Two mechanisms were generally proposed for dendritic fragmentation, including remelting induced by solute enrichment and fragmentation due to stress concentration. However, it is generally believed that fragmentation due to pure bending or stress concentration is impossible because the ideal tensile stress of the material is very high [28]. In this study, the latter mechanism can be interpreted as fragmentation induced by fatigue stress. And it is extensively proved that a much lower stress is required to induce the crack when the material is against fatigue test rather than normal tensile test [29].

In this study, the stress acting on the arm by an interdendritic flow field can be estimated by equation (1) [28],

$$\sigma_x = \frac{6\mu v L^2}{r^3} \tag{1}$$

where r is the radius of primary or secondary dendrite root, v is the velocity of flow field induced by oscillated ultrasonic bubble (here the velocity of bubble wall was used), and L is the dendrite length. Using the parameters of arm 1 in Fig. 4 for the calculation, the stress is about ±3.97 kPa as $|v^+| = |v^-| = 0.46$ m/s [20], $r = 50$ μm, $L = 220$ μm. The calculated stress is much lower than the tensile strength of SCN [19]. However, as ultrasonic bubble oscillation continued, micro-cracks initiated at the roots of the dendrites and then propagated. The cyclic bending of a secondary arm at its root was always associated with stress concentration. After the detachment of the secondary arm, more area of the primary arm was exposed to the ultrasonic bubble ocsillaiton and the fluid convection. Accordingly, the scar left bt the fragmented secondary arm would become a weak point for the initiation of cracks due to stress concertation.

3.3. *The fatigue strength and fatigue life of the SCN dendrite in mushy zone*

3.3.1. *Pressure distribution in melt*

The fragmentation of solidified crystals in an ultrasound field was closely related to the ultrasonic pressure and interaction with the oscillating bubbles [18–20,21,25]. Wang et al. [25] found that the pressure amplitude induced by an oscillating bubble was at the same level as the fatigue stress of a Zn-4*wt.*%Al alloy. The pressure

distribution in the melt under experimental conditions was simulated by solving the Helmholtz equation (Eq. (2)) for ultrasonic pressure using software COMSOL Multiphysics (COMSOL, Inc., Burlington, MA) [19,25]. Table 1 listed the related properties and parameters of the alloy used in the experiment [30–34].

$$\frac{\kappa P_a}{\rho_0} + \nabla\cdot\left(\frac{1}{\rho_0}\nabla P_a\right) = 0 \tag{2}$$

where $\rho_0$is the liquid density, $\kappa = \omega/c_0$ is the wave number, and $\omega = 2\pi f$ is the angular frequency, f is the frequency of the sound wave, and c_0 is the traveling speed of sound in the liquid. The boundary conditions applied were (see Fig. 6a):

(1) Pressure source $P_a = P_A\cos(\omega t)$, at the surface of the sonotrode tip, where $P_A = \sqrt{2\rho_0 c_0 W/A}$ W is the ultrasonic power, and A is the sonotrode tip area;
(2) Sound hard boundary condition with zero normal derivative of the pressure $\partial P_a/\partial n = 0$ at the sides of the sonotrode;
(3) Sound soft boundary condition at the top end of domain to simulate the liquid/air interface ($P_a = 0$);
(4) Impedance, $Z = \rho\cdot c$ at liquid/glass interface.

Fig. 6a shows the instantaneous pressure distribution of a 2-D simulation under an ultrasonic power of 30 W at time $t = 0$ s. The pressure varied from −0.07 MPa to 5.18 MPa in the melt. Fig. 6b shows the pressure decreased exponentially along line 1 (vertical distance from tip, see Fig. 6a) and line 2 (horizontal distance from the sonotrode tip, see Fig. 6a). For line 1, the pressure reached 0.85 MPa at 5 mm from the sonotrode tip and decreased to −0.109 MPa at a minimum. However, the pressure reached −0.16 MPa at ~12.5 mm before it gradually recovered to zero at 20 mm from the tip. The pressure attenuation was due to the energy dissipation inside the liquid and the impedance at the liquid/glass interface.

The area marked inside the rectangular in Fig. 6a shows the area where the interaction between dendrites and bubbles was captured. As shown in Fig. 6b, the pressure mainly distributed in a range of −0.085 MPa to −0.02 MPa, and the average pressure was about −0.05Mpa. This pressure was used for further analysis of ultrasonic bubble dynamics.

Table 1
Physical properties of the succinonitrile-5wt. %Camphor [30–34].

Material	SCN-5*wt.* %Cam
Melting point, T_M	324.97 K
Density of liquid, $\rho_0^{\#}$	$0.970\times10^3\ kg\cdot m^{-3}$
Density of glass, ρ	$2.3\times10^3\ kg\cdot m^{-3}$
Viscosity of liquid, $\mu^{\#}$	$2.66\times10^{-3}\ Pa\cdot s$
Surface tension, $\sigma^{\#}$	$3.85\times10^{-2}\ N\cdot m^{-1}$
Empirical constant, B*	3046 atm
constant, n*	7.025
Ambient sound speed in liquid, c_0^*	$1450\ m\cdot s^{-1}$
Sound speed in glass, c	$2380\ m\cdot s^{-1}$
Gas polytrophic exponent γ	1.6 (for air)

Note: for the lack of data for molten SCN-5 *wt.* %Cam alloy, the values of ρ_0, μ, σ are the values of SCN; c_0, B, and n are the values of water.

3.3.2. Pressure amplitude of an oscillating ultrasonic bubble

The Gilmore model [35] was used to calculate the pressure evolution of an oscillating ultrasonic bubble according to Eqs. (3)–(6) using COMSOL Multiphysics. Fig. 7a shows the changes of bubble radius (initial diameter was 21.5 μm) versus the alternating ultrasonic pressure. The simulation configuration was similar to that in Fig. 6a with an ultrasonic power of 30 W. The amplitude of the ultrasonic pressure, i.e., P_A, was set as 0.05 MPa. Fig. 7b–d shows that the simulation result agreed quite well with experiment.

$$\left(1-\frac{\dot R}{C}\right)R\ddot R + \frac{3}{2}\dot R^2\left(1-\frac{\dot R}{3C}\right) = \left(1+\frac{\dot R}{C}\right)H + \frac{R\dot R}{C}\left(1-\frac{\dot R}{C}\right)\frac{dH}{dR} \tag{3}$$

$$C = \frac{n(P+B)}{\rho_0}\left(\frac{P+B}{P_0+B}\right)^{\frac{n-1}{2n}} \tag{4}$$

$$H = \frac{n}{n-1}\frac{(P_0+B)^{\frac{1}{n}}}{\rho}\left[(P+B)^{\frac{n-1}{n}} - (P_0+B)^{\frac{n-1}{n}}\right] \tag{5}$$

$$P(R) = \left(P_0 + \frac{2\sigma}{R_0}\right)\left(\frac{R_0}{R}\right)^{3\gamma} - \frac{2\sigma}{R} - \frac{4\mu\dot R}{R} \tag{6}$$

where R, P, H and C is the radius, pressure at the bubble wall, enthalpy and local speed of sound in the liquid, respectively; R_0 is the initial bubble radius, P_0 is the liquid ambient pressure at 1 atm and $P_\infty = P_0 + P_a$ is the pressure at infinite distance from the bubble. As the oscillation of a bubble is obtained, its pressure varying with

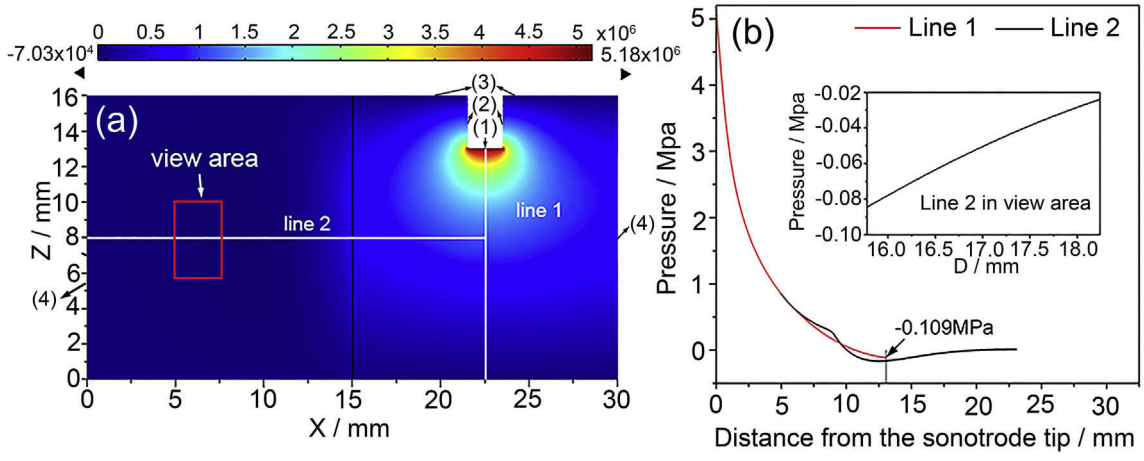

Fig. 6. (a) the simulated instantaneous pressure distribution in a 2-D domain under an ultrasonic power of 30 W and (b) the ultrasonic pressure distribution along line 1 and line 2.

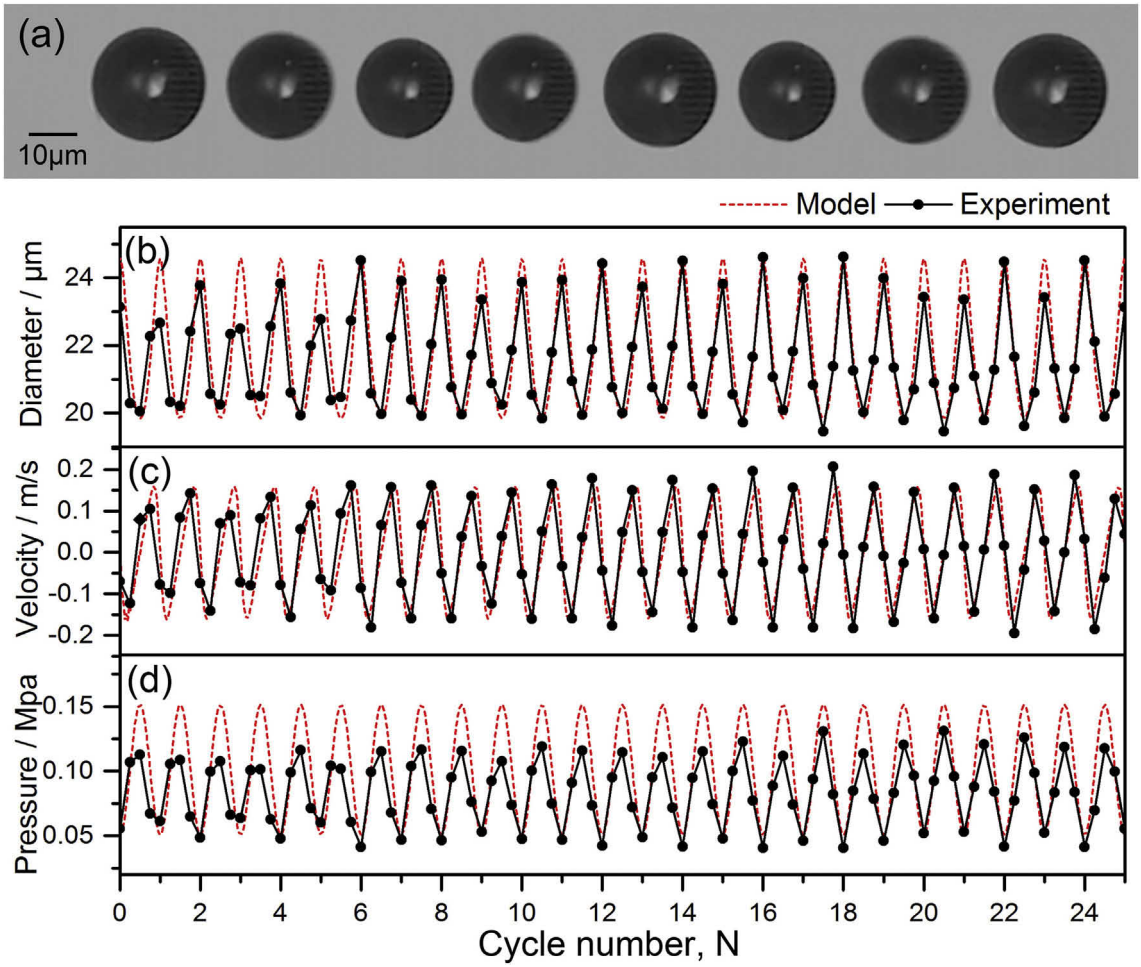

Fig. 7. (a) the oscillation of a quasi-steady state ultrasonic bubble captured near a dendrite boundary in experiment. (b)–(d) showed the diameter, velocity at bubble wall and pressure at bubble wall respectively. The red dashes were the simulated results with the ultrasonic pressure amplitude of about 0.05Mpa. The black lines were the measured diameters based on (a), the calculated (based on ultrasonic bubble diameter in experiment) velocity and pressure at the bubble wall. The ultrasonic power used was 30 W and the image acquisition rate was 80,000 *fps*. (For interpretation of the references to colour in this figure legend, the reader is referred to the Web version of this article.)

its diameter $P(R)$ can be calculated by Eq. (6).

3.3.3. Estimation of the fatigue stress

Table 2 lists the bubble diameter, pressure amplitude of the oscillating bubble and the fragmentation cycle number (the total cycle number for breaking a dendrite arm) extracted from Figs. 2–4. Fig. 8a shows the pressure profiles at a bubble wall calculated using the Gilmore model (maximum ultrasonic pressure amplitude was 0.05 MPa) corresponding to the conditions listed in Table 2.

According to Eqs. (7) and (8) [36], the values of lg$C$ and k are obtained as 8.49 and 0.96 respectively by a bilinear fitting of lg$S$ and lg$N$ (see Fig. 8b). The S-N curve for the dendrite in the mushy zone was calculated using Eq. (7). Accordingly, it can be estimated that the fatigue failure stress was below 1 MPa, which is consistent with that in Ref. [19].

$$N = CS^{-k} \tag{7}$$

$$\lg N = \lg C - k \lg S \tag{8}$$

We are aware that there are big differences in physical properties between metal and transparent alloys, hence, future work will be dedicated to study the interactions between ultrasonic bubbles and dendrites of metallic alloys. Nevertheless, using transparent alloys with ultrafast imaging is still a convenient and valuable method for revealing the highly dynamic phenomena concerning dendritic fragmentation due to ultrasound.

Table 2
Parameters related to dendrite fatigue under ultrasonic treatment.

Fragmented Dendrites	Bubble radium/μm	N, fragmentation cycle number	S, pressure amplitude/Mpa
Primary arm in Fig. 2	60	447	0.33982
Primary arm in Fig. 3a	15	1128	0.15852
Secondary arm 1 in Fig. 3b	40	808	0.21839
Secondary arm 2 in Fig. 4	10	1330	0.15807

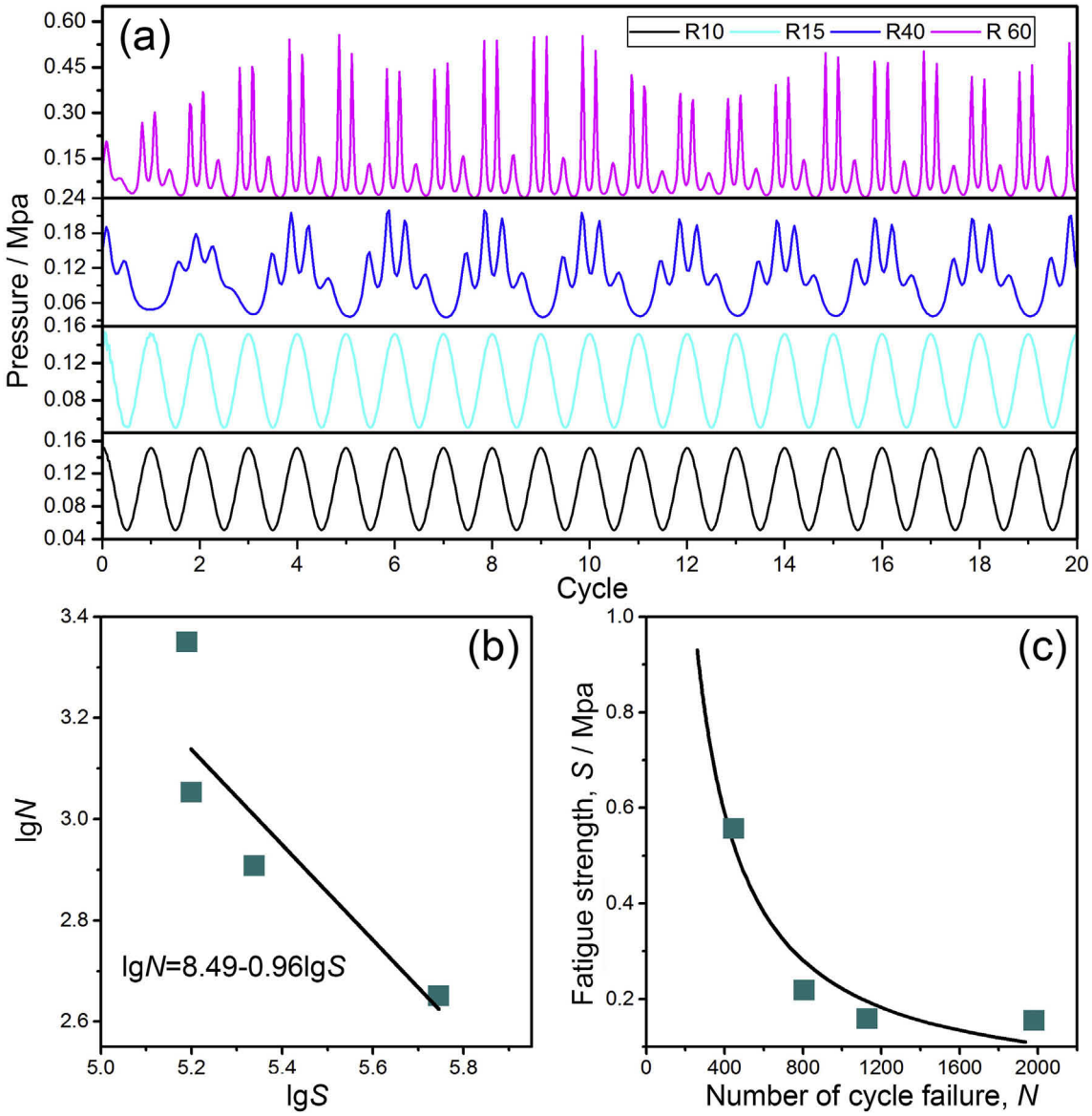

Fig. 8. (a) The pressure profiles at bubble wall calculated using the Gilmore model (the maximum ultrasonic pressure amplitude, 0.05 MPa) corresponding to the bubble conditions in Figs. 2–4. (b) The fitted plot of material constants lg *C* and *k* under different conditions based on Table 2. The solid lines are regression results according to the power law. (c) the *S-N* curves of SCN dendrite.

4. Conclusion

Dynamic interactions between growing dendrites of a SCN-5*wt.*% Camphor transparent alloy and quasi-static oscillating ultrasonic bubbles were studied systematically using high-speed imaging method. The experimental studies were complemented by calculating the evolution of bubble wall pressure and bubble radius using the Gilmore model. By viewing and analyzing hundreds and thousands of images, the following conclusions are drawn from this study:

(1) Cyclic pressure produced by quasi-steady state oscillating ultrasonic bubbles can exert a fatigue effect on growing dendrites, bending back and forth of the growing dendrites and initiating cracks at the dendrites roots. Propagation of the cracks can last for a few tens of milliseconds until complete fractures occur. With an ultrasonic power of 30 W in this experiment, the cyclic load generated by oscillating ultrasonic bubbles can fracture dendrites in less 50 ms.

(2) Based on the observed oscillating cycle number for fracturing dendrites due to the fatigue effect, the fatigue strength and fatigue life curve of SCN dendrites were calculated, and the stress for the fatigue failure of SCN dendrites was generally less than 1 MPa.

Acknowledgement

The authors would like to thank the Natural Science Foundation of China (No.51075299), the Tsinghua University Initiative Scientific Research Program (20151080370), and the UK Royal Society Newton International Fellowship Scheme for the financial support. J. Mi also would like to acknowledge the financial support from the UK Engineering and Physical Sciences Research Council (Grant No. EP/L019965/1) and the Royal Society Industry Fellowship in 2012–2016.

References

[1] G.I. Eskin, D.G. Eskin, Ultrasonic Treatment of Light Alloy Melts, second ed., CRC Press, Gordon and Breach, 2015.
[2] O.V. Abramov, High-intensity Ultrasonics: Theory and Industrial Applications, Gordon and Breach Science Publishers, Amsterdam, The Netherlands, 1998.
[3] Q. Han, Ultrasonic processing of materials, Metall. Mater. Trans. B 46 (2015) 1603–1614.
[4] Y. Xuan, L. Nastac, The role of ultrasonic cavitation in refining the microstructure of aluminum based nanocomposites during the solidification process, Ultrasonics 83 (2017) 94–102.
[5] X. Jian, H. Xu, T.T. Meek, Q. Han, Effect of power ultrasound on solidification of aluminum A356 alloy, Mater. Lett. 59 (2005) 190–193.
[6] J.D. Hunt, K.A. Jackson, Nucleation of solid in an undercooled liquid by cavitation, J. Appl. Phys. 37 (1966) 254–257.
[7] K. Yasuda, Y. Saiki, T. Kubo, M. Kuwabara, J. Yang, Influence of high-power ultrasonic irradiation on primary nucleation process during solidification, Jpn. J. Appl. Phys. 46 (2007) 4939–4944.
[8] G.I. Eskin, Effect of ultrasonic (cavitation) treatment of the melt on the microstructure evolution during solidification of aluminum alloy ingots, Z. Metallkd 93 (2002) 502–507.
[9] F. Wang, D. Eskin, J. Mi, T. Connolley, J. Lindsay, M. Mounib, A refining mechanism of primary Al_3 Ti intermetallic particles by ultrasonic treatment in the liquid state, Acta Mater. 116 (2016) 354–363.
[10] F. Wang, D. Eskin, T. Connolley, J. Mi, Effect of ultrasonic melt treatment on the refinement of primary Al3Ti intermetallic in an Al–0.4Ti alloy, J. Cryst. Growth 435 (2016) 24–30.
[11] T.V. Atamanenko, D.G. Eskin, L. Zhang, L. Katgerman, Criteria of grain refinement induced by ultrasonic melt treatment of aluminum alloys containing Zr and Ti, Metall. Mater. Trans. 41 (2010) 2056–2066.
[12] Z. Liu, D. Qiu, F. Wang, J.A. Taylor, M. Zhang, The grain refining mechanism of cast zinc through silver inoculation, Acta Mater. 79 (2014) 315–326.
[13] D. Ruvalcaba, R.H. Mathiesen, D.G. Eskin, L. Arnberg, L. Katgerman, In situ observations of dendritic fragmentation due to local solute-enrichment during directional solidification of an aluminum alloy, Acta Mater. 55 (2007) 4287–4292.
[14] T. Nagira, N. Nakatsuka, H. Yasuda, K. Uesugi, A. Takeuchi, Y. Suzuki, Impact of melt convection induced by ultrasonic wave on dendrite growth in Sn–Bi alloys, Mater. Lett. 150 (2015) 135–138.
[15] E. Liotti, A. Lui, R. Vincent, S. Kumar, Z. Guo, T. Connolley, I.P. Dolbnya, M. Hart, L. Arnberg, R.H. Mathiesen, A synchrotron X-ray radiography study of dendrite fragmentation induced by a pulsed electromagnetic field in an Al–15Cu alloy, Acta Mater. 70 (2014) 228–239.
[16] E. Liotti, A. Lui, S. Kumar, Z. Guo, C. Bi, T. Connolley, P.S. Grant, The spatial and temporal distribution of dendrite fragmentation in solidifying Al-Cu alloys under different conditions, Acta Mater. 121 (2016) 384–395.
[17] R. Chow, R. Blindt, R. Chivers, M. Povey, The sonocrystallisation of ice in sucrose solutions: primary and secondary nucleation, Ultrasonics 41 (2003) 595–604.
[18] R. Chow, R. Blindt, A. Kamp, P. Grocutt, R. Chivers, The microscopic visualisation of the sonocrystallisation of ice using a novel ultrasonic cold stage, Ultrason. Sonochem. 11 (2004) 245–250.
[19] D. Shu, B. Sun, J. Mi, P.S. Grant, A high-speed imaging and modeling study of dendrite fragmentation caused by ultrasonic cavitation, Metall. Mater. Trans. 43 (2012) 3755–3766.
[20] S. Wang, J. Kang, X. Zhang, Z. Guo, Dendrites fragmentation induced by oscillating cavitation bubbles in ultrasound field, Ultrasonics 83 (2018) 26–32.
[21] F. Wang, D. Eskin, J. Mi, C. Wang, B. Koe, A. King, C. Reinhard, T. Connolley, A synchrotron X-radiography study of the fragmentation and refinement of primary intermetallic particles in an Al-35Cu alloy induced by ultrasonic melt processing, Acta Mater. 141 (2017) 142–153.
[22] Z. Yang, C.G. Kang, Z.Q. Hu, Microstructural stress concentration: an important role in grain refinement of rheocasting structure, Metall. Mater. Trans. 36 (2005) 2785–2792.
[23] D.Y. Tan, J.W. Mi, High speed imaging study of the dynamics of ultrasonic bubbles at a liquid-solid interface, Mater. Sci. Forum 765 (2013) 230–234.
[24] F. Wang, I. Tzanakis, D. Eskin, J. Mi, T. Connolley, In situ observation of ultrasonic cavitation-induced fragmentation of the primary crystals formed in Al alloys, Ultrason. Sonochem. 39 (2017) 66–76.
[25] B. Wang, D. Tan, T.L. Lee, C.K. Jia, F. Wang, D. Eskin, T. Connolley, K. Fezzaa, J. Mi, Ultrafast synchrotron X-ray imaging studies of microstructure fragmentation in solidification under ultrasound, Acta Mater. 144 (2017) 505–515.
[26] T.L. Lee, J.C. Khong, K. Fezzaa, J.W. Mi, Ultrafast X-ray imaging and modelling of ultrasonic cavitations in liquid metal, Mater. Sci. Forum 765 (2013) 190–194.
[27] D. Tan, T.L. Lee, J.C. Khong, T. Connolley, K. Fezzaa, J. Mi, High-speed synchrotron X-ray imaging studies of the ultrasound shockwave and enhanced flow during metal solidification processes, Metall. Mater. Trans. B 46 (2015) 2851–2861.
[28] J. Pilling, A. Hellawell, Mechanical deformation of dendrites by fluid flow, Metall. Mater. Trans. 27 (1996) 229–232.
[29] S. Suresh, Fatigue of Materials, second ed., Cambridge University Press, Cambridge, 1998.
[30] K. Somboonsuk, J.T. Mason, R. Trivedi, Interdendritic spacing: Part I. Experimental studies, Metall. Mater. Trans. 15 (1984) 967–975.
[31] A. Ludwig, W. Kurz, Direct observation of solidification microstructures around absolute stability, Acta Mater. 44 (1996) 3643–3654.
[32] J. Holzfuss, M. Ruggeberg, A. Billo, Shock wave emissions of a sonoluminescing bubble, Phys. Rev. Lett. 81 (1998) 5434–5437.
[33] J. Teng, S. Liu, Re-determination of succinonitrile (SCN)-camphor phase diagram, J. Cryst. Growth 290 (2006) 248–257.
[34] S. Akamatsu, H. Nguyen-Thi, In situ observation of solidification patterns in diffusive conditions, Acta Mater. 108 (2016) 325–346.
[35] F.R. Gilmore, The growth or collapse of a spherical bubble in a viscous compressible liquid, Calif. Inst. Tech Eng. Rep. 26 (1952) 1–40.
[36] S. Nagarjuna, M. Srinivas, K. Balasubramanian, D.S. Sarmat, Effect of alloying content on high cycle fatigue behaviour of Cu-Ti alloys, Int. J. Fatig. 19 (1997) 51–57.